AGU PUBLICATIONS

Geophysical Research Letters

RESEARCH LETTER
10.1002/2016GL067785

Key Points:
- The M_w 7.2 earthquake ruptured unilaterally to the northwest lasting 40 s
- Early aftershocks were triggered within 2 min occurring near the subduction interface
- A seaward-intraplate strike-slip earthquake triggered landward-intraplate earthquakes

Supporting Information:
- Texts S1 and S2 and Figures S1–S9

Correspondence to:
W. Fan,
w3fan@ucsd.edu

Citation:
Fan, W., and P. M. Shearer (2016), Fault interactions and triggering during the 10 January 2012 M_w 7.2 Sumatra earthquake, *Geophys. Res. Lett.*, *43*, 1934–1942, doi:10.1002/2016GL067785.

Received 14 JAN 2016
Accepted 18 FEB 2016
Accepted article online 19 FEB 2016
Published online 8 MAR 2016

Fault interactions and triggering during the 10 January 2012 M_w 7.2 Sumatra earthquake

Wenyuan Fan[1] and Peter M. Shearer[1]

[1] Scripps Institution of Oceanography, University of California, San Diego, La Jolla, California, USA

Abstract The 10 January 2012 M_w 7.2 Sumatra earthquake in the Wharton basin occurred 3 months before the great M_w 8.6 and M_w 8.2 earthquakes in the same region, which had complex ruptures and are the largest strike-slip earthquakes ever recorded. Teleseismic *P* wave back projection of the M_w 7.2 earthquake images a unilateral rupture lasting ~40 s without observable frequency dependency (low frequency, 0.05–0.3 Hz, high frequency, 0.3–1 Hz). In addition to radiation bursts during the M_w 7.2 main shock, coherent energy releases from 50 to 75 s and from 100 to 125 s are observed about 143 km northeast of the main shock rupture and landward of the trench. Analysis of globally recorded *P* waves, in both 0.02–0.05 Hz velocity records and 1–5 Hz stacked envelope functions, confirms the presence of coherent sources during the time windows. The observed energy bursts are likely to be large early aftershocks occurring on or near the subduction interface. Both dynamic and static triggering could have induced these early aftershocks, as they initiated after the surface wave passed by, and the Coulomb stress perturbations from the M_w 7.2 main shock promote earthquakes in the observed locations. The earthquake sequence is a clear example of a seaward-intraplate strike-slip earthquake triggering landward-intraplate earthquakes in the same region, in contrast to previously reported normal-reverse or reverse-normal interactions at subduction zones.

1. Introduction

Large earthquakes often involve complex fault interactions, in which ruptures can jump fault boundaries and trigger earthquakes not directly connected to the main shock. Both static and dynamic stress changes promote triggered earthquakes over a wide range of spatial and temporal scales [e.g., *Harris*, 1998; *Kilb et al.*, 2000; *Kilb*, 2003; *Lin and Stein*, 2004; *Toda et al.*, 2005]. For earthquakes occurring in active tectonic regions, multiple fault segments can rupture simultaneously or sequentially [e.g., *Wald and Heaton*, 1994; *Ji et al.*, 2002a; *Wei et al.*, 2011; *Yue et al.*, 2012; *Uchide et al.*, 2013]. At subduction zones, interactions among seaward-intraplate, landward-intraplate, and interplate faults often exhibit complex relationships [e.g., *Lay et al.*, 2009; *Li et al.*, 2009; *Ye et al.*, 2012; *Ruiz and Contreras-Reyes*, 2015]. The northwest Sunda arc subduction zone is of particular current interest because five $M_w > 8$ earthquakes have struck the region since 2004, beginning with the massive M_w 9.2 2004 Sumatra earthquake. The Indo-Australian plate deforms as multiple rigid units [*Minster and Jordan*, 1978], which might be responsible for the intricate intraplate and subduction earthquakes of the region [e.g., *Robinson et al.*, 2001; *Abercrombie et al.*, 2003; *Antolik et al.*, 2006]. Therefore, understanding interactions among these faults is of great interest as a potential clue to infer seismic properties of the Sunda megathrust.

In 2012, three large strike-slip earthquakes with global centroid moment tensor (GCMT) magnitude [*Ekström et al.*, 2012] M_w 7.2, M_w 8.6, and M_w 8.2, reactivated old fracture zones and seafloor fabrics west of the Sumatra trench beneath the Wharton basin (Figure 1). Source models of the M_w 8.6 earthquake indicate the event ruptured at least four faults over 160 s [e.g., *Wang et al.*, 2012; *Yue et al.*, 2012; *Satriano et al.*, 2012; *Meng et al.*, 2012; *Zhang et al.*, 2012; *Ishii et al.*, 2013; *Wei et al.*, 2013; *Hill et al.*, 2015]. The M_w 8.2 earthquake struck 2 h later, and the M_w 7.2 earthquake occurred 3 months prior to the M_w 8.6 earthquake. The epicenters of the M_w 7.2 foreshock and M_w 8.6 main shock are ~30 km away (Figure 1) [*International Seismological Centre*, 2013]. The hypocenter depths are 20.9 km and 26.3 km for the M_w 7.2 foreshock and M_w 8.6 main shock [*International Seismological Centre*, 2013], while the GCMT centroid depths vary from 23.7 km to 45.6 km, respectively [*Ekström et al.*, 2012]. Aside from the location differences, the initial 15 s of the far-field recorded *P* waves of these two earthquakes bear few similarities (Figure S1 in the supporting information). The dissimilar initial

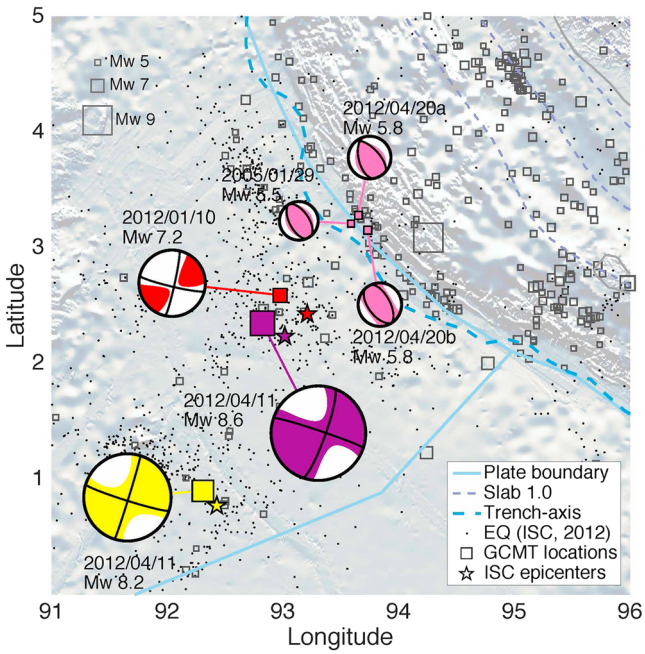

Figure 1. Tectonic setting of the 2012 Sumatra earthquake sequence. The 2012 M_w 7.2, M_w 8.6, and M_w 8.2 strike-slip earthquakes are shown with their epicenters, GCMT locations, and GCMT focal mechanisms. Three reverse-faulting M5 earthquakes are shown with their centroid locations and GCMT focal mechanisms, which are ~100 km away from the M_w 7.2 earthquake. Black dots are earthquakes from 1 year (2012) of International Seismological Centre catalog of the Sumatra region [*International Seismological Centre*, 2013]. Squares are events from the GCMT catalog of the region since 1979. The plate boundary is from *Bird* [2003], trench axis is from *Bassett and Watts* [2015a, 2015b], and the subduction geometry is from Slab 1.0 with 20 km separation [*Hayes et al.*, 2012]. The background bathymetry gradient is from *Sandwell et al.* [2014] and *Garcia et al.* [2014].

P waves and the location offsets of these two earthquakes suggest they might not have ruptured the same fault, as the fossil Wharton ridges can potentially form a set of strike-parallel fault systems in the region [*Singh et al.*, 2011].

Here we examine the M_w 7.2 earthquake with far-field global and array seismic records. Using *P* wave back projection, we resolve that the quake ruptured unilaterally for about 40 s, propagating northwest. The results reveal a similar rupture pattern for two frequency bands (low frequency, 0.05–0.3 Hz, high frequency, 0.3–1 Hz). In addition, at 50 to 75 s and 100 to 125 s, we image coherent energy radiation originating landward of the trench, about 143 km northeast of the main shock rupture. The coherent energy radiators indicate triggering of large early aftershocks near the subduction interface. The imaged early aftershocks are also seen in global *P* waves in both 0.02–0.05 Hz velocity records and 1–5 Hz stacked envelope functions. The detected earthquake sequence is a rare case of seaward-intraplate strike-slip earthquake triggering landward-intraplate earthquakes, suggesting long-range fault interactions in the region.

2. The 10 January 2012 M_w 7.2 Sumatra Earthquake

Great strike-slip earthquakes are rare and often involve perplexing rupture complexities [e.g., *Ji et al.*, 2002a; *Bouchon and Vallée*, 2003; *Dunham and Archuleta*, 2004; *Vallée et al.*, 2008; *Walker and Shearer*, 2009; *Robinson*, 2011; *Kennett et al.*, 2014]. The 2012 Sumatra strike-slip earthquake sequence is particularly intriguing. First, the M_w 8.6 and M_w 8.2 quakes are the two largest strike-slip earthquakes that have been instrumentally recorded [*Meng et al.*, 2012; *Duputel et al.*, 2012]. Second, the sequence happened beneath the Wharton basin, which is considered to be a diffuse deformation zone that is separating the Indian and Australian Plates [*Wiens et al.*, 1985; *Delescluse and Chamot-Rooke*, 2007; *DeMets et al.*, 2010]. Third, the centroid depths, including a M_w 6.2 aftershock (15 April 2012), are all deeper than 20 km [*Ekström et al.*, 2012; *Wei et al.*, 2013], suggesting the earthquakes occurred primarily in the mantle. The M_w 7.2 Sumatra earthquake occurred west of Northern Sumatra and 423 km SW of Banda Aceh, Indonesia (2.43°N, 93.21°E, 20.9 km) [*International Seismological Centre*, 2013]. The GCMT [*Ekström et al.*, 2012] source solution has strike 103°, dip 81°, and rake

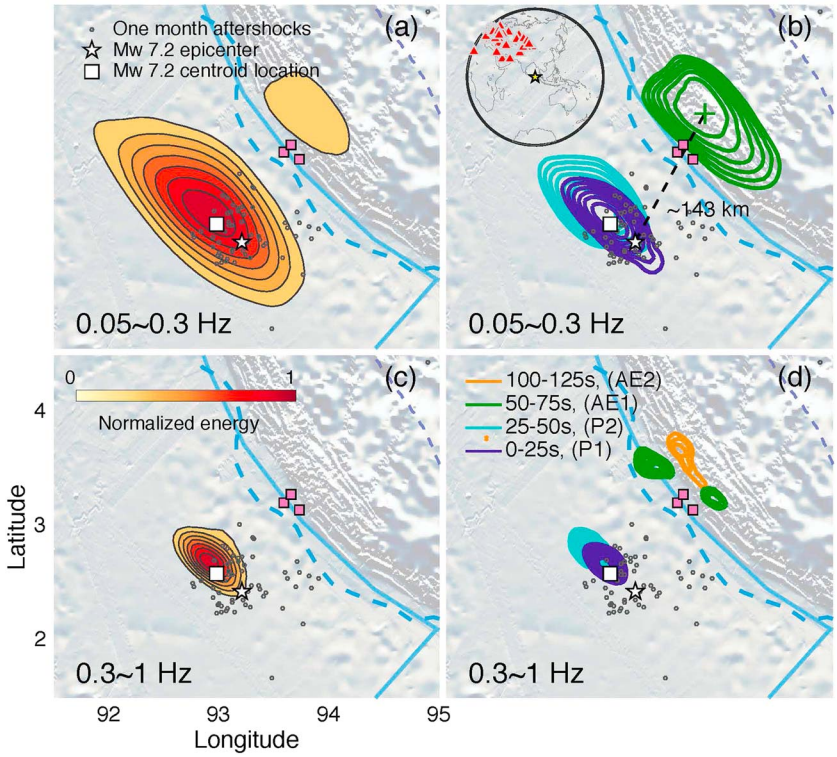

Figure 2. Back projection results from European stations. (a) Low-frequency (LF, 0.05–0.3 Hz) time-integrated back projection image. (b) Low-frequency (LF, 0.05–0.3 Hz) rupture evolution. (c) High-frequency (HF, 0.3–1 Hz) time-integrated back projection image. (d) High-frequency (HF, 0.3–1 Hz) rupture evolution. Two energy bursts from 0 to 50 s are denoted as P1 and P2. The two energy bursts shown at 50 to 75 s and 100 to 125 s are likely from one or more triggered events, shown in the maps northeast of the trench, and not physically connected to the main shock rupture. They are denoted as AE1 and AE2. The insert in Figure 2b shows the stations used for back projection of the M_w 7.2 earthquake.

−173°. The finite-fault model from the U.S. Geological Survey National Earthquake Information Center (NEIC), based on a W-Phase moment tensor solution, has strike 101.2° and dip 75.1° [*Duputel et al.*, 2011; *Hayes*, 2011; *Hayes et al.*, 2011; *Ji et al.*, 2002b]. The finite-fault model suggests most of the displacement on the fault slipped above the hypocenter, and the moment rate function derived from the finite-fault model shows the rupture lasted for about 40 s.

P wave back projection [e.g., *Ishii et al.*, 2005; *Walker et al.*, 2005; *Walker and Shearer*, 2009; *Koper et al.*, 2011; *Kiser and Ishii*, 2012; *Yagi et al.*, 2012] is useful for resolving the spatiotemporal evolution of complicated earthquakes because it makes few prior assumptions about the fault geometry. The method has been successfully applied in mapping out complex ruptures [e.g., *Kiser and Ishii*, 2011; *Fan and Shearer*, 2015] and in detecting subevents and early aftershocks [e.g., *Yao et al.*, 2012; *Kiser and Ishii*, 2013]. Here we apply a variation of the back projection approach we used to image the 2015 Nepal earthquake [*Fan and Shearer*, 2015] to the 2012 M_w 7.2 Sumatra earthquake using teleseismic *P* wave vertical-component velocity records. Because of the less ideal azimuthal coverage of stations for the Sumatra event, and to avoid potential back projection artifacts due to polarity flips caused by focal mechanism rotations or differences during the rupture, we restrict our analysis to 89 stations located in Europe (Figure 2) and the Hi-net array located in Japan (Figures S2 and S3) [*Okada et al.*, 2004; *Obara et al.*, 2005]. We grid the potential sources at 5 km spacing, within the latitude range 0.6° to 4.2° and longitude range 91.4° to 95.0° (400 km by 400 km). Following *Xu et al.* [2009] and *Fan and Shearer* [2015], we filter the *P* waves into two frequency bands, 0.05–0.3 Hz (low frequency, LF) and 0.3–1 Hz (high frequency, HF), to assess possible frequency dependence in the seismic radiation images. Details about the back projection method and data processing are presented in the supporting information. No postsmoothing or postprocessing is applied to the images.

From integrated back projection images over ~125 s (Figure 2), the earthquake does not show frequency-dependent rupture behavior. Most of the radiated energy was released northwest of the epicenter

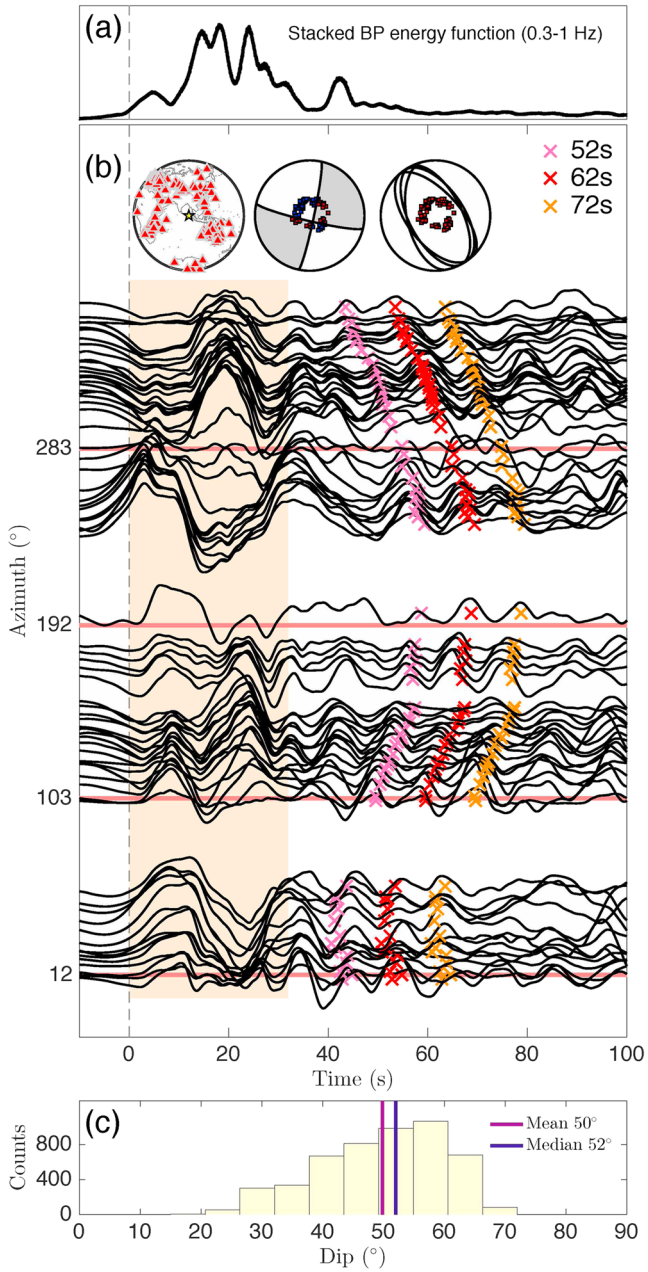

Figure 3. (a) Stacked Back-projection (BP) energy function at 0.3–1 Hz. The function is a self-normalized stack of all the back projected seismograms in the source region. (b) Aligned velocity seismograms (low frequency, 0.02–0.05 Hz) from global stations with predicted traveltime arrivals of AE1 in Figure 2. Station map shown as left-upper corner insert, the polarities of the M_w 7.2 strike-slip GCMT focal mechanism shown as middle insert, and the polarities of the M5 reverse-faulting GCMT focal mechanisms shown as right insert (Red, positive polarity; Blue, negative polarity). The records are sorted by azimuth. Colored crosses show predicted arrival with AE1 location at three different rupture times. (c) Dip distribution of grid-searched focal mechanisms from the HASH algorithm.

with a concentration around the GCMT centroid location. Both LF and HF back projection snapshots imply a northwest unilateral rupture (0 to 25 s is denoted as P1, 25 to 50 s is denoted as P2, Figures 2b and 2d), lasting for ~40 s (Figure 3a). The snapshots show a compact rupture around the epicenter as suggested by the NEIC finite-fault model. From 50 to 75 s (AE1) and 100 to 125 s (AE2), additional coherent energy bursts are observed landward of the plate boundary [*Bird*, 2003] and trench axis [*Bassett and Watts*, 2015a, 2015b], well eastward of the main shock rupture (~143 km, Figures 2 and S3). The clear spatial separation between the first 50 s and the later energy bursts indicates the landward energy release comes from aftershocks.

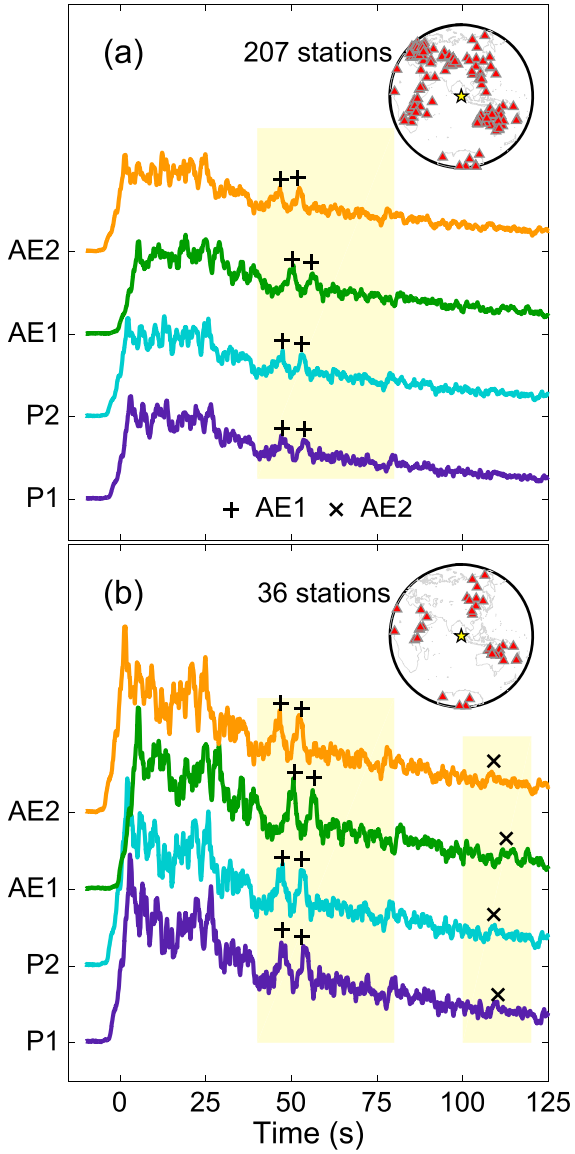

Figure 4. (a) Stacked envelope functions of P1, P2, AE1, and AE2 in Figure 2, station map plotted as right-upper corner insert. The *P* wave seismograms are filtered at 1–5 Hz. The envelope functions are calculated with a standard Hilbert transform without smoothing. (b) Same as Figure 4a with stations within 20° azimuth of the M_w 7.2 main shock W-phase nodal planes. Peaks related to AE1 are labeled as plus. Peaks related to AE2 are labeled as cross.

This landward region hosted three M5 earthquakes (Figures 1 and 2) with reverse-faulting focal mechanisms before and after the M_w 7.2 quake, suggesting the region is capable of accumulating enough strain for earthquakes and the observed early aftershocks might share similar focal mechanisms with the M5 earthquakes. Analysis of far-field very long period seismic waves (first 5400 s, 2 mHz to 5 mHz) does not require a second source to explain the data, which suggests the magnitudes of the early aftershocks are significantly smaller than the M_w 7.2 main shock (Figure S4).

Theoretical resolution kernels, back projection of a M_w 5.9 earthquake in the same region, and synthetic tests with depth phases indicate that these early aftershock images are well resolved and distinct from the main shock (Figures S5 and S6). To further validate that they are true features, we examine globally recorded far-field *P* waves (i.e., not just the European stations used for the back projection) in two frequency bands beyond the bands used for back projection (0.02–0.05 Hz, Figure 3 and 1–5 Hz, Figure 4). We first azimuthally align the 0.02–0.05 Hz globally recorded *P* waves with empirical time-shift corrections [*Houser et al.*, 2008], then stack the self-normalized records within each 2° azimuthal bin, and finally normalize the stacks with station

numbers used for stacking of each bin (Figure 3b). The aligned stacks show clear polarity shifts for the first 40 s at azimuths of ~12°, ~103°, ~192°, and ~283°, agreeing well with the moment tensor solutions [*Ekström et al.*, 2012; *Duputel et al.*, 2011]. If the observed early aftershocks in Figure 2 can be approximated as point sources, globally recorded seismograms should show energy pulses at the predicted arrival times from the 1-D velocity model used for back projection (IASP91) [*Kennett and Engdahl*, 1991]. With the peak energy burst location of 50 to 75 s (AE1), we then try to find the best rupture time that can explain the aligned seismograms. The theoretical arrivals from the inferred AE1 location with rupture times 52, 62, and 72 s are shown as colored crosses (Figure 3b). The early aftershock AE1 can explain the pulses in the stacks at most azimuths (Figure 3b), having an apparent duration of 20 s. The pulses associated with AE1 all share the same positive polarities, suggesting the focal mechanisms of the early aftershocks are likely reverse faulting rather than strike-slip faulting (Figure 3b). Assuming the positive polarities are shared by all the stations, we implemented HASH [*Hardebeck and Shearer*, 2002, 2003] to grid search 5000 possible focal mechanisms of AE1. Limited by the station distribution, possible focal mechanisms are poorly determined with only polarity information. Resolved dips range from 18° to 72°, with mean and median 50° and 52°, respectively (Figure 3c). Strikes cannot be determined, and rakes are consistent with a reverse-faulting focal mechanism. For the focal mechanisms of the three M5 earthquakes (Figure 3b, insert), the predicted polarities of all the stations are positive, which further supports the likely reverse-faulting focal mechanism of the observed early aftershocks.

To test for coherent high-frequency energy bursts, we stacked envelope functions from 207 globally recorded *P* waves, filtered at 1 – 5 Hz (Figure 4a). To account for time shifts due to differing source locations, the envelope functions are time shifted using the predicted arrivals of each target energy burst location before stacking (P1 and P2 for the first 50 s; AE1 and AE2 for 50 to 75 s and 100 to 125 s). The stacked function is then normalized with the station number. Although main shock coda decay dominates the stacks, clear pulses in the stacked envelope functions can be identified in the 50 to 75 s window (Figure 4a). To reduce the strength of the main shock coda, we experimented with restricting the stack to records from the subset of stations that are near the main shock *P* wave nodal planes. When using only stations within 20° of the W-phase CMT nodal planes (36 stations), the 50 to 75 s pulses are more distinct in the stacked envelope functions (Figure 4b) and an additional pulse near 110 s can be identified (Figure 4b), confirming the 100 to 125 s energy burst observed in Figure 2d. Two nearby GEOFON stations (≤5°) have *S* wave arrivals in their smoothed envelope functions at the time of the two early aftershocks (Figure S6), preventing their detection of AE1 and AE2.

The observed energy bursts (Figure 2) are unlikely to be artifacts or due to water phases. Because of the 25 s stacking window length, the depth phases do not bias the results very much (Figure S7). Water phases would be insignificant for the M_w 7.2 Sumatra earthquake because of the large depth and the shallow water layer of the region [*Wiens*, 1989]. Complex water reverberations usually show strong azimuthal dependence [*Chu et al.*, 2011], which is not observed in this case (Figure 4b). Finally, global *P* wave spectra of the earthquake do not show resonance-frequency signatures due to a finite water layer (Figure S8) [*Zhan et al.*, 2014].

3. Faulting Interactions

The detected early aftershocks (Figure 2, 3, and 4) could have been triggered by both dynamic and static triggering. Because the spatial separation between the M_w 7.2 main shock and the early aftershocks is around 143 km, strong near-field seismic waves can potentially activate the fault systems close to the trench, while the static stress changes could influence the systems as well [e.g., *Kilb*, 2003; *Lin and Stein*, 2004]. Such correlated seismic activities between fault systems have been observed in other trench areas, for example, the Kuril Islands [*Ammon et al.*, 2008], Japan trench [*Lay et al.*, 2013], Philippine trench [*Ye et al.*, 2012], and northern Tonga [*Li et al.*, 2009].

Rapid onset dynamic aftershock triggering usually coincides with large-amplitude seismic wave arrivals, for example, surface waves [e.g., *Kilb et al.*, 2000]. Assuming the local surface wave speed is ~3 km/s, the distance and the timing of AE1 (~143 km, ~50 s) strongly correlate with the surface wave arrivals. The distances from AE1 to the later parts of the M_w 7.2 rupture range from ~141 to ~145 km (Figure 5), extending the shaking in the landward region around AE1 for about 40 s.

The static stress changes could either promote or prohibit aftershocks, depending on the local Coulomb stress changes [e.g., *Lin and Stein*, 2004; *Toda et al.*, 2005]. With the NEIC finite-fault source model, we compute Coulomb stress changes induced on shallow reverse-faulting geometries (e.g., the nearby M_w 5.5, 29 January 2005, M_w 5.8 doublet, 20 April 2012, Figures 5 and S9), as suggested by the polarity analysis (Figure 3).

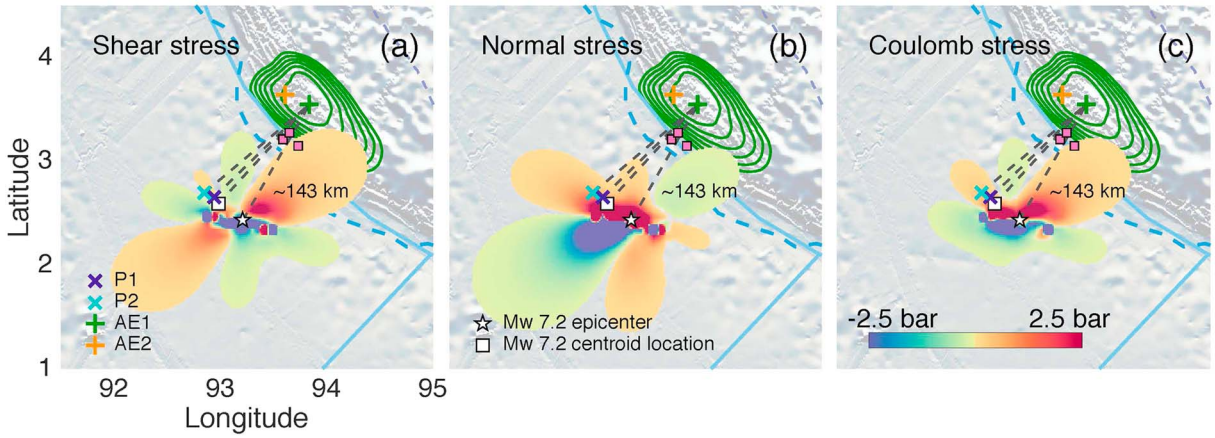

Figure 5. Horizontal cross sections of (a) shear stress, (b) normal stress, and (c) Coulomb stress changes at 20 km. The stress changes are calculated from the main shock NEIC finite-fault model on a target reverse fault 332°/48°/97° (strike/dip/rake) of 20 April 2012b, M_w 5.8, using the Coulomb 3 software [*Lin and Stein*, 2004; *Toda et al.*, 2005]. Distances from AE1 to M_w 7.2 epicenter, centroid location, P1, and P2 ranges from ~141 km to ~145 km.

In Figure 5, shear stress, normal stress, and Coulomb stress are calculated with Young's modulus 8.0×10^5 Pa, friction coefficient 0.4, and receiving fault geometry 332°/48°/97° (strike/dip/rake) of 20 April 2012b, M_w 5.8 (Figure 1) at a depth of 20 km. Stress contours of Figure 5 show areas where the stress changes exceed 10 kPa. The Coulomb stress increase positively correlates with where we locate the early aftershocks (Figures 5 and S9), indicating static stress changes might be part of the driving forces triggering these events. However, the static Coulomb stress increase might be insufficient to induce fault failure for certain focal mechanisms (Figure S9a), leaving the importance of static stress triggering undetermined.

The 2012 seismicity of the region [*International Seismological Centre*, 2013] shows a high density of seismicity where we observe the early aftershocks (Figure 1). The GCMT catalog [*Ekström et al.*, 2012] has a large concentration of seismicity close to the Sumatra trench (Figure 1), showing the trench region is capable of hosting moderate earthquakes frequently. If the early aftershocks we observed in Figures 2 and 3 share similar focal mechanisms of the 29 January 2005 M_w 5.5 earthquake or the 20 April 2012 M_w 5.8 doublet (Figure 1), the steep dipping angles of the nodal planes suggest it is unlikely for the early aftershocks to occur at the shallowest portion of the megathrust. More likely, these events are intraplate earthquakes near the subducting slab. The landward seismicities in Figure 1 are mostly aftershocks of the M_w 8.6 earthquake, suggesting it might be common for seaward-intraplate earthquakes to trigger landward-intraplate earthquakes in this region.

4. Conclusions

As revealed by teleseismic *P* wave back projection, the 10 January 2012 M_w 7.2 Sumatra earthquake unilaterally ruptured northwest for about 40 s. We apply regional seismic network (European array) back projection to both low-frequency (LF, 0.05–0.3 Hz) and high-frequency (HF, 0.3–1 Hz) data to evaluate the energy radiation. Both frequency bands reveal similar rupture behavior, showing no frequency dependence. Besides the relatively compact rupture pattern around the hypocenter, there are coherent energy bursts at 50 to 75 s and 100 to 125 s observed landward of the trench. Combining global *P* wave velocity records (0.02–0.05 Hz) and 1–5 Hz stacked *P* wave envelope functions, we infer the observed energy bursts are early aftershocks rupturing within 2 min of the main shock. Both dynamic triggering and Coulomb stress perturbations over the region may have contributed to the occurrence of the early aftershocks. Our observations indicate that seaward-intraplate strike-slip earthquakes can trigger landward-intraplate reverse-faulting earthquakes in this part of the Sunda arc. Because such early aftershocks may be difficult to detect within the coda of larger earthquakes, it is unclear how commonly such triggering occurs.

Acknowledgments
The seismic data from networks, AF, AU, CH, CZ, DK, ER, G, GE, GR, GT, IC, II, IM, IU, KC, KN, KR, KZ, MN, ND, NL, OE, PL, PS, RO, TW, XV, and ZM were provided by Data Management Center (DMC) of the Incorporated Research Institutions for Seismology (IRIS) and National Research Institute for Earth Science Disaster Prevention in Japan (NIED). Coulomb 3 software was developed by S. Toda, R. Stein, J. Lin, and V. Sevilgen. The earthquake catalog was downloaded from the International Seismological Center (ISC). The bathymetry data were processed with the Generic Mapping Tools (GMT) [*Wessel and Smith*, 1991; *Wessel et al.*, 2013]. This work was supported by National Science Foundation grant EAR-1111111. The authors thank the Editor, Andrew V. Newman, reviewer, Claudio Satriano, and one anonymous reviewer for their suggestions that improved the quality of the manuscript.

References

Abercrombie, R. E., M. Antolik, and G. Ekström (2003), The June 2000 Mw 7.9 earthquakes south of Sumatra: Deformation in the India–Australia plate, *J. Geophys. Res., 108*(B1), 2018, doi:10.1029/2001JB000674.

Ammon, C. J., H. Kanamori, and T. Lay (2008), A great earthquake doublet and seismic stress transfer cycle in the central Kuril islands, *Nature, 451*(7178), 561–565.

Antolik, M., R. E. Abercrombie, J. Pan, and G. Ekström (2006), Rupture characteristics of the 2003 Mw 7.6 mid–Indian ocean earthquake: Implications for seismic properties of young oceanic lithosphere, *J. Geophys. Res.*, *111*, B04302, doi:10.1029/2005JB003785.

Bassett, D., and A. B. Watts (2015a), Gravity anomalies, crustal structure, and seismicity at subduction zones: 1. Seafloor roughness and subducting relief, *Geochem. Geophys. Geosyst.*, *16*, 1508–1540, doi:10.1002/2014GC005684.

Bassett, D., and A. B. Watts (2015b), Gravity anomalies, crustal structure, and seismicity at subduction zones: 2. Interrelationships between fore-arc structure and seismogenic behavior, *Geochem. Geophys. Geosyst.*, *16*, 1541–1576, doi:10.1002/2014GC005685.

Bird, P. (2003), An updated digital model of plate boundaries, *Geochem. Geophys. Geosyst.*, *4*(3), 1027, doi:10.1029/2001GC000252.

Bouchon, M., and M. Vallée (2003), Observation of long supershear rupture during the magnitude 8.1 Kunlunshan earthquake, *Science*, *301*(5634), 824–826, doi:10.1126/science.1086832.

Chu, R., S. Wei, D. V. Helmberger, Z. Zhan, L. Zhu, and H. Kanamori (2011), Initiation of the great Mw 9.0 Tohoku–Oki earthquake, *Earth Planet. Sci. Lett.*, *308*(3–4), 277–283, doi:10.1016/j.epsl.2011.06.031.

Delescluse, M., and N. Chamot-Rooke (2007), Instantaneous deformation and kinematics of the India–Australia plate, *Geophys. J. Int.*, *168*(2), 818–842, doi:10.1111/j.1365-246X.2006.03181.x.

DeMets, C., R. G. Gordon, and D. F. Argus (2010), Geologically current plate motions, *Geophys. J. Int.*, *181*(1), 1–80, doi:10.1111/j.1365-246X.2009.04491.x.

Dunham, E. M., and R. J. Archuleta (2004), Evidence for a supershear transient during the 2002 Denali fault earthquake, *Bull. Seismol. Soc. Am.*, *94*(6B), S256–S268, doi:10.1785/0120040616.

Duputel, Z., L. Rivera, H. Kanamori, G. P. Hayes, B. Hirshorn, and S. Weinstein (2011), Real-time W–phase inversion during the 2011 off the Pacific coast of Tohoku earthquake, *Earth Planets Space*, *63*(7), 535–539, doi:10.5047/eps.2011.05.032.

Duputel, Z., H. Kanamori, V. C. Tsai, L. Rivera, L. Meng, J.-P. Ampuero, and J. M. Stock (2012), The 2012 Sumatra great earthquake sequence, *Earth Planet. Sci. Lett.*, *351–352*, 247–257, doi:10.1016/j.epsl.2012.07.017.

Ekström, G., M. Nettles, and A. Dziewoński (2012), The global CMT project 2004-2010: Centroid-moment tensors for 13,017 earthquakes, *Phys. Earth Planet. Inter.*, *200–201*, 1–9, doi:10.1016/j.pepi.2012.04.002.

Fan, W., and P. Shearer (2015), Detailed rupture imaging of the 25 April 2015 Nepal earthquake using teleseismic *P* waves, *Geophys. Res. Lett.*, *42*, 5744–5752, doi:10.1002/2015GL064587.

Garcia, E. S., D. T. Sandwell, and W. H. Smith (2014), Retracking Cryosat-2, Envisat and Jason-1 radar altimetry waveforms for improved gravity field recovery, *Geophys. J. Int.*, *196*(3), 1402–1422, doi:10.1093/gji/ggt469.

Hardebeck, J. L., and P. M. Shearer (2002), A new method for determining first-motion focal mechanisms, *Bull. Seismol. Soc. Am.*, *92*(6), 2264–2276, doi:10.1785/0120010200.

Hardebeck, J. L., and P. M. Shearer (2003), Using S/P amplitude ratios to constrain the focal mechanisms of small earthquakes, *Bull. Seismol. Soc. Am.*, *93*(6), 2434–2444, doi:10.1785/0120020236.

Harris, R. A. (1998), Introduction to special section: Stress triggers, stress shadows, and implications for seismic hazard, *J. Geophys. Res.*, *103*(B10), 24,347–24,358, doi:10.1029/98JB01576.

Hayes, G. P. (2011), Rapid source characterization of the 2011 M_w 9.0 off the Pacific coast of Tohoku earthquake, *Earth Planets Space*, *63*(7), 529–534, doi:10.5047/eps.2011.05.012.

Hayes, G. P., P. S. Earle, H. M. Benz, D. J. Wald, and R. W. Briggs (2011), 88 hours: The U.S. Geological Survey National Earthquake Information Center response to the 11 March 2011 M_w 9.0 Tohoku earthquake, *Seismol. Res. Lett.*, *82*(4), 481–493, doi:10.1785/gssrl.82.4.481.

Hayes, G. P., D. J. Wald, and R. L. Johnson (2012), Slab1.0: A three-dimensional model of global subduction zone geometries, *J. Geophys. Res.*, *117*, B01302, doi:10.1029/2011JB008524.

Hill, E. M., et al. (2015), The 2012 M_w8.6 Wharton basin sequence: A cascade of great earthquakes generated by near-orthogonal, young, oceanic mantle faults, *J. Geophys. Res. Solid Earth*, *120*, 3723–3747, doi:10.1002/2014JB011703.

Houser, C., G. Masters, P. Shearer, and G. Laske (2008), Shear and compressional velocity models of the mantle from cluster analysis of long-period waveforms, *Geophys. J. Int.*, *174*(1), 195–212, doi:10.1111/j.1365-246X.2008.03763.x.

International Seismological Centre (2013), On-line Bulletin. Int. Seis. Cent., Thatcham, U. K. [Available at http://www.isc.ac.uk.]

Ishii, M., P. M. Shearer, H. Houston, and J. E. Vidale (2005), Extent, duration and speed of the 2004 Sumatra-Andaman earthquake imaged by the Hi-net array, *Nature*, *435*(7044), 933–936.

Ishii, M., E. Kiser, and E. L. Geist (2013), Mw 8.6 Sumatran earthquake of 11 April 2012: Rare seaward expression of oblique subduction, *Geology*, *41*(3), 319–322, doi:10.1130/G33783.1.

Ji, C., D. J. Wald, and D. V. Helmberger (2002a), Source description of the 1999 Hector mine, California, earthquake, Part II: Complexity of slip history, *Bull. Seismol. Soc. Am.*, *92*(4), 1208–1226, doi:10.1785/0120000917.

Ji, C., D. J. Wald, and D. V. Helmberger (2002b), Source description of the 1999 Hector Mine, California, earthquake, Part I: Wavelet domain inversion theory and resolution analysis, *Bull. Seismol. Soc. Am.*, *92*(4), 1192–1207.

Kennett, B. L. N., and E. R. Engdahl (1991), Traveltimes for global earthquake location and phase identification, *Geophys. J. Int.*, *105*(2), 429–465, doi:10.1111/j.1365-246X.1991.tb06724.x.

Kennett, B. L. N., A. Gorbatov, and S. Spiliopoulos (2014), Tracking high-frequency seismic source evolution: 2004 Mw 8.1 Macquarie event, *Geophys. Res. Lett.*, *41*, 1187–1193, doi:10.1002/2013GL058935.

Kilb, D. (2003), A strong correlation between induced peak dynamic Coulomb stress change from the 1992 M7.3 Landers, California, earthquake and the hypocenter of the 1999 M7.1 Hector Mine, California, earthquake, *J. Geophys. Res.*, *108*(B1), 2012, doi:10.1029/2001JB000678.

Kilb, D., J. Gomberg, and P. Bodin (2000), Triggering of earthquake aftershocks by dynamic stresses, *Nature*, *408*(6812), 570–574.

Kiser, E., and M. Ishii (2011), The 2010 Mw 8.8 Chile earthquake: Triggering on multiple segments and frequency-dependent rupture behavior, *Geophys. Res. Lett.*, *38*, L07301, doi:10.1029/2011GL047140.

Kiser, E., and M. Ishii (2012), Combining seismic arrays to image the high-frequency characteristics of large earthquakes, *Geophys. J. Int.*, *188*(3), 1117–1128, doi:10.1111/j.1365-246X.2011.05299.x.

Kiser, E., and M. Ishii (2013), Hidden aftershocks of the 2011 Mw 9.0 Tohoku, Japan earthquake imaged with the back-projection method, *J. Geophys. Res. Solid Earth*, *118*, 5564–5576, doi:10.1002/2013JB010158.

Koper, K. D., A. H. T. Lay, C. Ammon, and H. Kanamori (2011), Frequency-dependent rupture process of the 2011 Mw 9.0 Tohoku earthquake: Comparison of short-period *P* wave backprojection images and broadband seismic rupture models, *Earth Planets Space*, *63*(7), 599–602.

Lay, T., H. Kanamori, C. J. Ammon, A. R. Hutko, K. Furlong, and L. Rivera (2009), The 2006–2007 Kuril islands great earthquake sequence, *J. Geophys. Res.*, *114*, B11308, doi:10.1029/2008JB006280.

Lay, T., Z. Duputel, L. Ye, and H. Kanamori (2013), The December 7, 2012 Japan trench intraplate doublet (Mw 7.2, 7.1) and interactions between near-trench intraplate thrust and normal faulting, *Phys. Earth Planet. Inter.*, *220*, 73–78, doi:10.1016/j.pepi.2013.04.009.

Li, X., G. Shao, and C. Ji (2009), Rupture process of Mw 8.1 Samoa earthquake constrained by joint inverting teleseismic body, surface waves and local strong motion, *Eos Trans. AGU*, *90*(52), Fall Meet. Suppl., Abstract U21D–03.
Lin, J., and R. S. Stein (2004), Stress triggering in thrust and subduction earthquakes and stress interaction between the southern San Andreas and nearby thrust and strike-slip faults, *J. Geophys. Res.*, *109*, B02303, doi:10.1029/2003JB002607.
Meng, L., J.-P. Ampuero, J. Stock, Z. Duputel, Y. Luo, and V. C. Tsai (2012), Earthquake in a maze: Compressional rupture branching during the 2012 Mw 8.6 Sumatra earthquake, *Science*, *337*(6095), 724–726, doi:10.1126/science.1224030.
Minster, J. B., and T. H. Jordan (1978), Present-day plate motions, *J. Geophys. Res.*, *83*(B11), 5331–5354, doi:10.1029/JB083iB11p05331.
Obara, K., K. Kasahara, S. Hori, and Y. Okada (2005), A densely distributed high-sensitivity seismograph network in Japan: Hi-net by National Research Institute for Earth Science and Disaster Prevention, *Rev. Sci. Instrum.*, *76*(2), 021301, doi:10.1063/1.1854197.
Okada, Y., K. Kasahara, S. Hori, K. Obara, S. Sekiguchi, H. Fujiwara, and A. Yamamoto (2004), Recent progress of seismic observation networks in Japan—Hi-net, F-net, K-net and KIK-net, *Earth Planets Space*, *56*(8), 15–28, doi:10.1186/BF03353076.
Robinson, D. P. (2011), A rare great earthquake on an oceanic fossil fracture zone, *Geophys. J. Int.*, *186*(3), 1121–1134, doi:10.1111/j.1365-246X.2011.05092.x.
Robinson, D. P., C. Henry, S. Das, and J. H. Woodhouse (2001), Simultaneous rupture along two conjugate planes of the Wharton basin earthquake, *Science*, *292*(5519), 1145–1148, doi:10.1126/science.1059395.
Ruiz, J. A., and E. Contreras-Reyes (2015), Outer rise seismicity boosted by the Maule 2010 Mw 8.8 megathrust earthquake, *Tectonophysics*, *653*, 127–139, doi:10.1016/j.tecto.2015.04.007.
Sandwell, D. T., R. D. Müller, W. H. F. Smith, E. Garcia, and R. Francis (2014), New global marine gravity model from Cryosat-2 and Jason-1 reveals buried tectonic structure, *Science*, *346*(6205), 65–67, doi:10.1126/science.1258213.
Satriano, C., E. Kiraly, P. Bernard, and J.-P. Vilotte (2012), The 2012 Mw 8.6 Sumatra earthquake: Evidence of westward sequential seismic ruptures associated to the reactivation of a N-S ocean fabric, *Geophys. Res. Lett.*, *39*, L15302, doi:10.1029/2012GL052387.
Singh, S. C., H. Carton, A. S. Chauhan, S. Androvandi, A. Davaille, J. Dyment, M. Cannat, and N. D. Hananto (2011), Extremely thin crust in the Indian ocean possibly resulting from plume–ridge interaction, *Geophys. J. Int.*, *184*(1), 29–42, doi:10.1111/j.1365-246X.2010.04823.x.
Toda, S., R. S. Stein, K. Richards-Dinger, and S. B. Bozkurt (2005), Forecasting the evolution of seismicity in southern California: Animations built on earthquake stress transfer, *J. Geophys. Res.*, *110*, B05S16, doi:10.1029/2004JB003415.
Uchide, T., H. Yao, and P. M. Shearer (2013), Spatio-temporal distribution of fault slip and high-frequency radiation of the 2010 El Mayor-Cucapah Mexico earthquake, *J. Geophys. Res. Solid Earth*, *118*, 1546–1555, doi:10.1002/jgrb.50144.
Vallée, M., M. Landès, N. M. Shapiro, and Y. Klinger (2008), The 14 November 2001 Kokoxili (Tibet) earthquake: High-frequency seismic radiation originating from the transitions between sub-Rayleigh and supershear rupture velocity regimes, *J. Geophys. Res.*, *113*, B07305, doi:10.1029/2007JB005520.
Wald, D. J., and T. H. Heaton (1994), Spatial and temporal distribution of slip for the 1992 Landers, California, earthquake, *Bull. Seismol. Soc. Am.*, *84*(3), 668–691.
Walker, K. T., and P. M. Shearer (2009), Illuminating the near-sonic rupture velocities of the intracontinental Kokoxili Mw 7.8 and Denali fault Mw 7.9 strike-slip earthquakes with global *P* wave back projection imaging, *J. Geophys. Res.*, *114*, B02304, doi:10.1029/2008JB005738.
Walker, K. T., M. Ishii, and P. M. Shearer (2005), Rupture details of the 28 March 2005 Sumatra Mw 8.6 earthquake imaged with teleseismic *P* waves, *Geophys. Res. Lett.*, *32*, L24303, doi:10.1029/2005GL024395.
Wang, D., J. Mori, and T. Uchide (2012), Supershear rupture on multiple faults for the Mw 8.6 Off Northern Sumatra, Indonesia earthquake of April 11, 2012, *Geophys. Res. Lett.*, *39*, L21307, doi:10.1029/2012GL053622.
Wei, S., et al. (2011), Superficial simplicity of the 2010 El Mayor-Cucapah earthquake of Baja California in Mexico, *Nat. Geosci.*, *4*(9), 615–618.
Wei, S., D. Helmberger, and J.-P. Avouac (2013), Modeling the 2012 Wharton basin earthquakes off-Sumatra: Complete lithospheric failure, *J. Geophys. Res. Solid Earth*, *118*, 3592–3609, doi:10.1002/jgrb.50267.
Wessel, P., and W. H. Smith (1991), Free software helps map and display data, *Eos Trans. AGU*, *72*(441), 445–446.
Wessel, P., W. H. F. Smith, R. Scharroo, J. Luis, and F. Wobbe (2013), Generic mapping tools: Improved version released, *Eos Trans. AGU*, *94*(45), 409–410, doi:10.1002/2013EO450001.
Wiens, D. A. (1989), Bathymetric effects on body waveforms from shallow subduction zone earthquakes and application to seismic processes in the Kurile trench, *J. Geophys. Res.*, *94*(B3), 2955–2972, doi:10.1029/JB094iB03p02955.
Wiens, D. A., et al. (1985), A diffuse plate boundary model for Indian ocean tectonics, *Geophys. Res. Lett.*, *12*(7), 429–432, doi:10.1029/GL012i007p00429.
Xu, Y., K. D. Koper, O. Sufri, L. Zhu, and A. R. Hutko (2009), Rupture imaging of the Mw 7.9 12 May 2008 Wenchuan earthquake from back projection of teleseismic *P* waves, *Geochem. Geophys. Geosyst.*, *10*, Q04006, doi:10.1029/2008GC002335.
Yagi, Y., A. Nakao, and A. Kasahara (2012), Smooth and rapid slip near the Japan trench during the 2011 Tohoku-Oki earthquake revealed by a hybrid back-projection method, *Earth Planet. Sci. Lett.*, *355–356*, 94–101, doi:10.1016/j.epsl.2012.08.018.
Yao, H., P. M. Shearer, and P. Gerstoft (2012), Subevent location and rupture imaging using iterative back-projection for the 2011 Tohoku M_W 9.0 earthquake, *Geophys. J. Int.*, *190*(2), 1152–1168, doi:10.1111/j.1365-246X.2012.05541.x.
Ye, L., T. Lay, and H. Kanamori (2012), Intraplate and interplate faulting interactions during the August 31, 2012, Philippine trench earthquake (M_W 7.6) sequence, *Geophys. Res. Lett.*, *39*, L24310, doi:10.1029/2012GL054164.
Yue, H., T. Lay, and K. D. Koper (2012), En echelon and orthogonal fault ruptures of the 11 April 2012 great intraplate earthquakes, *Nature*, *490*(7419), 245–249.
Zhan, Z., V. C. Tsai, J. M. Jackson, and D. Helmberger (2014), Ambient noise correlation on the Amery Ice Shelf, East Antarctica, *Geophys. J. Int.*, *196*(3), 1796–1802, doi:10.1093/gji/ggt488.
Zhang, H., J. Chen, and Z. Ge (2012), Multi-fault rupture and successive triggering during the 2012 Mw 8.6 Sumatra offshore earthquake, *Geophys. Res. Lett.*, *39*, L22305, doi:10.1029/2012GL053805.